ACS APPLIED MATERIALS & INTERFACES

www.acsami.org

Research Article

Nanorod-Structured $NiCo_2O_4$/Moss-Like $Ni(OH)_2$ Composites with Enhanced Capacitive Performance for Photorechargeable Devices

Changhua Mi, Haowei Yu, Yudong Han, Yiqi Wang, Cewen Xin, Jiahao Yang, Jingang Guo, Jianan Gu, Yanlong Lv, Yanhong Wang, Xin Sun,* and Meicheng Li*

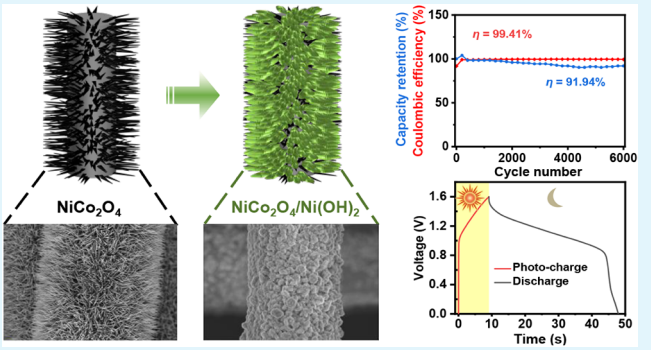
Cite This: *ACS Appl. Mater. Interfaces* 2026, 18, 32546−32556

Read Online

ACCESS | Metrics & More | Article Recommendations | Supporting Information

Downloaded via BEIJING NORMAL UNIV on June 18, 2026 at 09:53:22 (UTC).
See https://pubs.acs.org/sharingguidelines for options on how to legitimately share published articles.

ABSTRACT: Nickel hydroxide, $Ni(OH)_2$, is regarded as an attractive electrode material for supercapacitors, owing to its high theoretical specific capacitance, low cost, and facile preparation. However, its capacitive performance is limited by low conductivity, sluggish ion diffusion kinetics, and poor structural stability. In this work, we systematically regulate the nanostructure of $NiCo_2O_4$/$Ni(OH)_2$ composites, which significantly enhances the capacitive properties of $Ni(OH)_2$, providing a promising energy storage material for photorechargeable devices. The nanorod-structured $NiCo_2O_4$ with a high specific surface area facilitates rapid electron transfer and provides abundant sites for $Ni(OH)_2$ loading. Notably, the cetyltrimethylammonium bromide (CTAB)-induced porous $Ni(OH)_2$ grows continuously and uniformly over the $NiCo_2O_4$ framework, allowing more materials to be utilized for energy storage. Furthermore, the robust $NiCo_2O_4$ nanorods serve as a structural backbone, effectively suppressing the pulverization and detachment of the $Ni(OH)_2$ during prolonged cycling. The results show that the composite electrodes exhibit a specific capacitance of 2170.22 F/g (301.42 mAh/g) at 1 A/g and a capacitance retention of 82.3% at 20 A/g, with the assembled supercapacitor maintaining 91.94% of its initial capacitance after 6000 cycles at 2 A/g. Benefiting from the improved performance, particularly the rate capability, the resulting photorechargeable supercapacitors achieve a solar-to-electrochemical energy efficiency of 16.21%. This study provides a nanostructure engineering strategy for improving the capacitive behaviors of materials, advancing high-performance photorechargeable devices.



KEYWORDS: *$NiCo_2O_4$/$Ni(OH)_2$, nanostructure engineering, morphology control, Ni-based supercapacitors, photorechargeable devices*

1. INTRODUCTION

Supercapacitors hold a crucial role in electrochemical energy storage due to their low cost, high safety, and long cycle life.[1,2] Among them, pseudocapacitive supercapacitors, which employ battery-type materials as energy storage electrodes, store energy through Faradaic reactions. Compared to electric double-layer capacitors, they exhibit significantly higher specific capacitance and energy density.[1] Moreover, pseudocapacitive supercapacitors (hereafter referred to as supercapacitors) possess remarkable capabilities for high-power charging/discharging and dynamic fast response,[3] making them attractive candidates for smoothing the intermittency and fluctuation of solar energy.[4,5] By integrating supercapacitors with photovoltaic modules (photorechargeable devices), the dependence of electronic devices on frequent manual charging can also be significantly mitigated, facilitating a transition toward fully self-sufficient energy systems.[6,7] However, the efficiency of current photorechargeable devices remains significantly lower than that of standalone photovoltaic modules, which makes the performance optimization of the energy storage module a primary research focus.[8−10] Since the electrochemical properties of the device are governed by the active materials used in the storage module, the development of high-performance (e.g., high capacitance and high-rate capability) electrodes remains a key challenge.[11−14]

Representative electrode materials for supercapacitors include conductive polymers, transition metal oxides/sulfides, and hydroxides.[15,16] Among these materials, $Ni(OH)_2$ is considered one of the most promising candidates for large-scale applications due to its intrinsic properties, such as high theoretical specific capacitance and low cost.[17] However, pristine $Ni(OH)_2$ electrodes exhibit high internal resistance, sluggish reaction kinetics, and poor structural stability, which prevents them from meeting expectations.[18,19] To address these drawbacks, various modification strategies including

Received: February 7, 2026
Revised: May 27, 2026
Accepted: May 31, 2026
Published: June 8, 2026



ACS Publications

© 2026 American Chemical Society

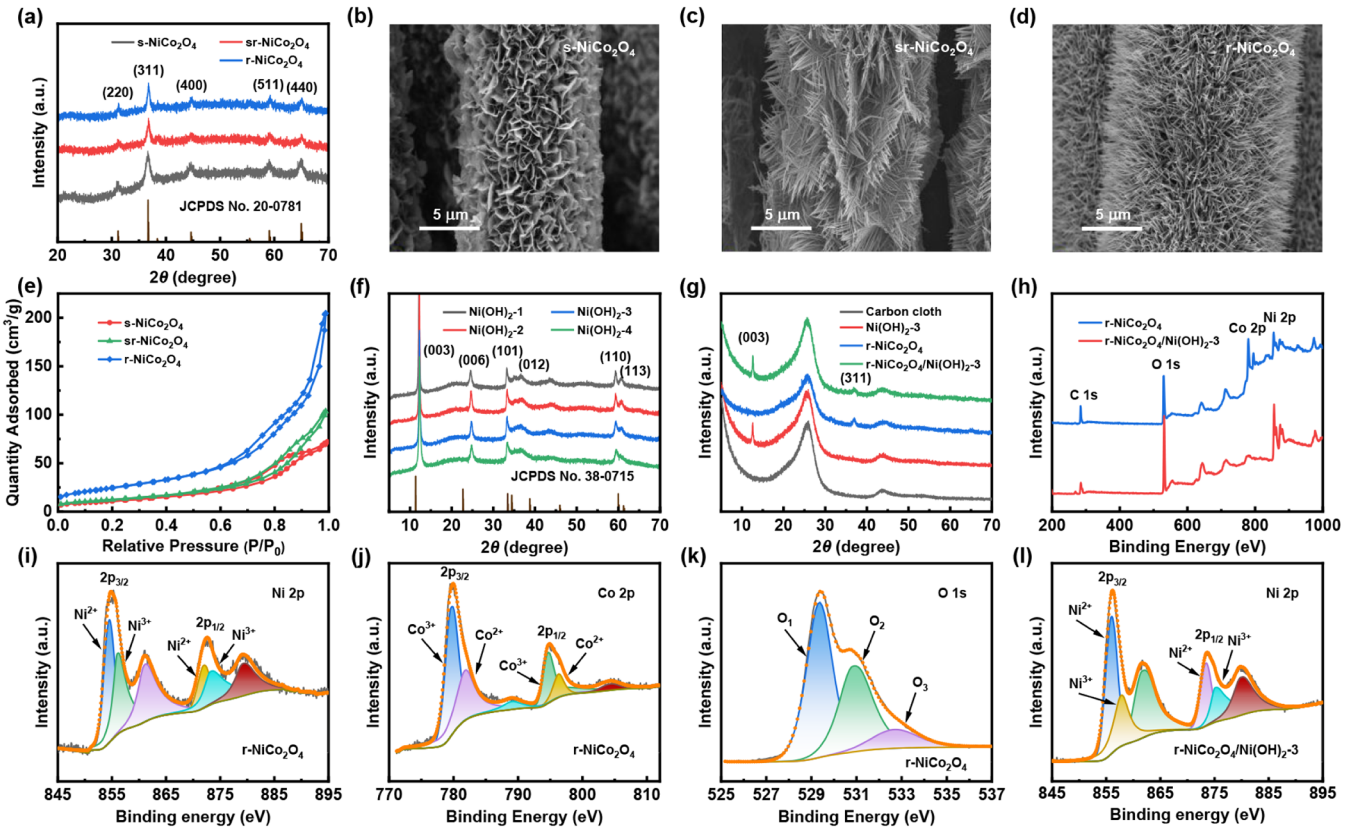


Figure 1. (a) XRD patterns of $NiCo_2O_4$ powders with different morphologies. (b–d) SEM images of various $NiCo_2O_4$ grown on carbon cloth. (e) Nitrogen adsorption–desorption isotherms of $NiCo_2O_4$ powders with different morphologies. (f) XRD patterns of $Ni(OH)_2$ powders synthesized at different precursor concentrations. (g) XRD patterns of $Ni(OH)_2$-3, r-$NiCo_2O_4$, and r-$NiCo_2O_4$/$Ni(OH)_2$-3 grown on carbon cloth. (h) XPS survey spectra of r-$NiCo_2O_4$ and r-$NiCo_2O_4$/$Ni(OH)_2$-3 grown on carbon cloth. (i–k) High-resolution XPS spectra of Ni 2p, Co 2p, and O 1s for r-$NiCo_2O_4$. (l) High-resolution XPS spectrum of Ni 2p for r-$NiCo_2O_4$/$Ni(OH)_2$-3.

elemental doping, composite construction, and structural regulation have been adopted to optimize $Ni(OH)_2$ materials, resulting in significant performance improvements.[1,18] In particular, constructing composites effectively increases the specific surface area of materials and optimizes the distribution of electroactive sites for Faradaic reactions.[1,20−22] Composite electrodes composed of ternary metal oxides (such as $MnCo_2O_4$, $ZnCo_2O_4$ and $NiCo_2O_4$) and $Ni(OH)_2$ demonstrate superior capacitive performance.[18,23] $NiCo_2O_4$ is prioritized as a highly promising material, largely due to its exceptional electrical conductivity.[24] The abundant porous architecture of $NiCo_2O_4$/$Ni(OH)_2$ composites maximizes the effective contact area between the electrode and electrolyte, while providing additional active sites for energy storage reactions, thereby enhancing the utilization efficiency of the electrode material.[25−27] Additionally, the core–shell architecture formed by $NiCo_2O_4$ and $Ni(OH)_2$ reduces the agglomeration and restacking of $Ni(OH)_2$, which greatly improves the cycling stability of the supercapacitor.[28] The hierarchical core–shell structure also effectively mitigates the poor conductivity of $Ni(OH)_2$, thereby enhancing its specific capacitance.[29,30] Nevertheless, both $NiCo_2O_4$ and $Ni(OH)_2$ can exhibit diverse micromorphologies, such as nanosheets, nanorods, and spherical-like structures.[31−34] The roles of these varying morphologies on the capacitive properties of $NiCo_2O_4$/$Ni(OH)_2$ composites are yet to be fully elucidated, calling for further systematic investigation to optimize their performance.

In this work, the capacitive performance of $NiCo_2O_4$/$Ni(OH)_2$ composites is significantly enhanced via nanostructure engineering. Three distinct morphologies of $NiCo_2O_4$, including nanosheets (s-$NiCo_2O_4$), nanorods (r-$NiCo_2O_4$), and mixed nanosheets-nanorods (sr-$NiCo_2O_4$), were successfully synthesized by a facile hydrothermal method. Subsequently, the presynthesized $NiCo_2O_4$ architectures were individually integrated with a series of $Ni(OH)_2$ nanostructures, whose morphologies were modulated by CTAB and precursor concentrations. Electrochemical characterization reveals that the optimized sample, comprising moss-like $Ni(OH)_2$ integrated with nanorod-structured $NiCo_2O_4$, exhibits superior performance, which is attributed to the well-matched nanostructures and the maximized electrochemically active surface area. The composite electrodes deliver a specific capacitance of 2170.22 F/g at 1 A/g, substantially surpassing that of pristine $Ni(OH)_2$. Their rate capability is also greatly boosted, as evidenced by a capacitance retention of 82.3% at 20 A/g. This enhanced rate capability is essential to accommodate the high-current output characteristics of photovoltaics. Furthermore, the assembled $NiCo_2O_4$/$Ni(OH)_2$//AC supercapacitor retains 91.94% of its initial specific capacitance after 6000 galvanostatic charge–discharge (GCD) cycles. Finally, the as-prepared supercapacitors were integrated with passivated emitter and rear cell (PERC) photovoltaic modules, forming an attractive photorechargeable supercapacitor with an overall efficiency of 16.21% under AM 1.5G illumination.

https://doi.org/10.1021/acsami.6c02790
ACS Appl. Mater. Interfaces 2026, 18, 32546−32556

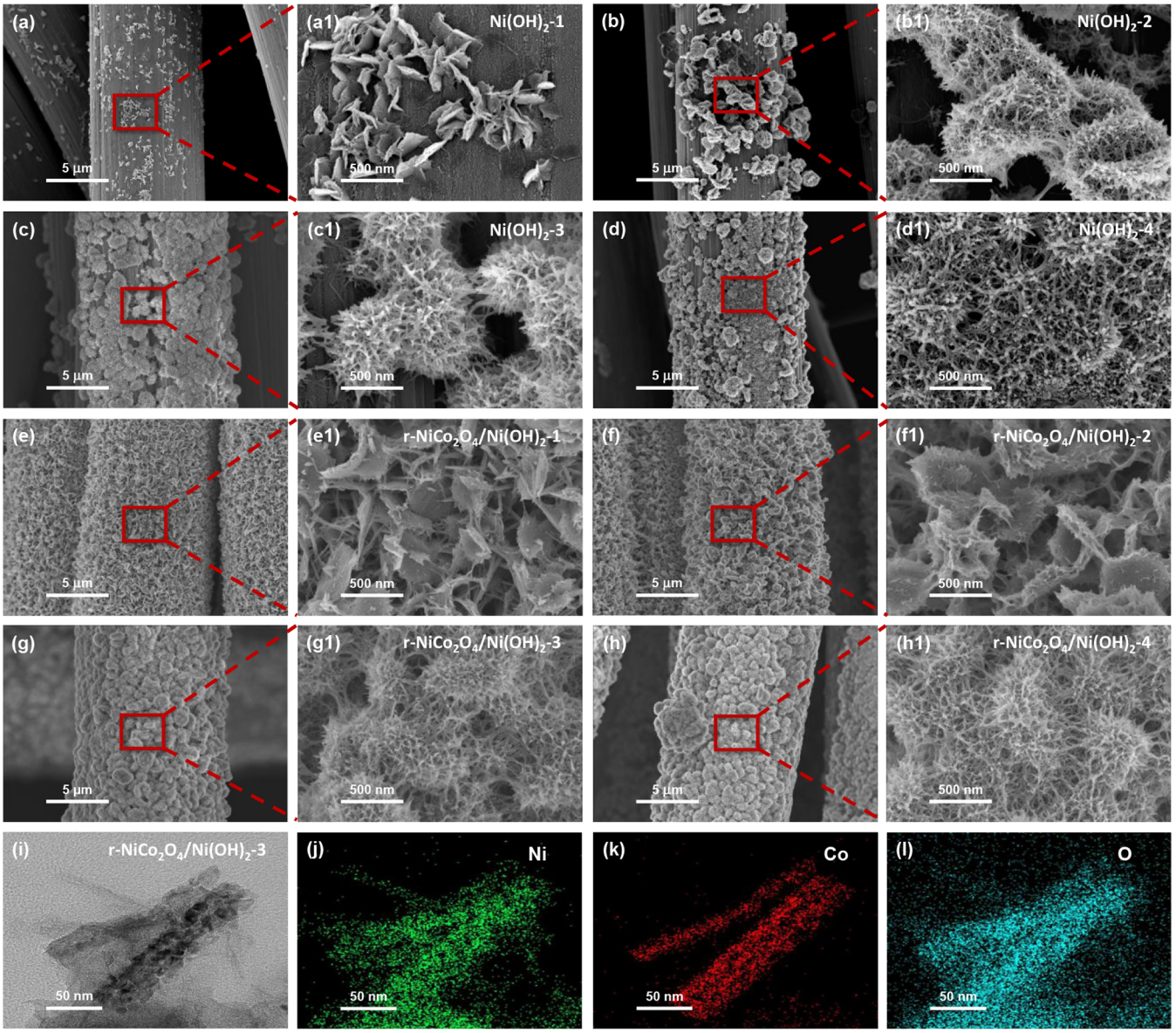


Figure 2. (a–d) SEM images of $Ni(OH)_2$ directly grown on carbon cloth at different precursor concentrations. (e–h) SEM images of $Ni(OH)_2$ grown on r-$NiCo_2O_4$ at different precursor concentrations. (a1–h1) Corresponding magnified SEM views. (i) TEM image of r-$NiCo_2O_4$/$Ni(OH)_2$-3. (j–l) Corresponding EDS elemental mapping of Ni, Co, and O.

2. RESULTS AND DISCUSSION

2.1. Structural and Morphological Characterization

The X-ray diffraction (XRD) patterns of $NiCo_2O_4$ with various morphologies are displayed in Figure 1a. All samples exhibit identical diffraction profiles, where the peaks can be clearly indexed to the cubic spinel phase of $NiCo_2O_4$ (JCPDS No. 20-0781).[35] The scanning electron microscopy (SEM) images in Figure 1b–d illustrate the three distinct morphologies of $NiCo_2O_4$, with corresponding high-magnification views provided in Figure S1. It can be observed that the s-$NiCo_2O_4$, composed of nanosheets, is uniformly and densely loaded onto the carbon cloth. Its nanosheets are interlaced and randomly oriented, forming a honeycomb-like open network with abundant voids. The sr-$NiCo_2O_4$ exhibits a hierarchical nanosheet-nanorod hybrid structure. In this architecture, the nanosheets act as a structural backbone, while the nanorods are grown in an interwoven manner across the nanosheet surfaces. As for the r-$NiCo_2O_4$, it consists of high-density and well-aligned nanorods that radially cover the carbon cloth. These nanorods exhibit a test tube brush-like morphology, maintaining significant voids between adjacent nanorods. The specific surface areas of the three $NiCo_2O_4$ powders were evaluated using N_2 adsorption–desorption measurements at 77 K. As shown in Figure 1e, all samples exhibit type-IV isotherms characteristic of mesoporous materials.[36,37] The Brunauer–Emmett–Teller (BET) analysis indicates that r-$NiCo_2O_4$ exhibits a specific surface area of 89.61 m^2/g, which is significantly higher than those of s-$NiCo_2O_4$ (40.35 m^2/g) and sr-$NiCo_2O_4$ (45.23 m^2/g). The high surface area is beneficial for increasing the interfacial contact with $Ni(OH)_2$, thereby facilitating charge transfer and enhancing electrochemical properties.[37,38] The $Ni(OH)_2$ samples, synthesized at four precursor concentrations (denoted as $Ni(OH)_2$-n, where a higher n represents an increased concentration; see Experimental Section for details), exhibit consistent crystalline

https://doi.org/10.1021/acsami.6c02790
ACS Appl. Mater. Interfaces 2026, 18, 32546–32556

phases, as confirmed by the XRD patterns in Figure 1f. All observed peaks can be indexed to the α-phase $Ni(OH)_2$ in accordance with JCPDS card No. 38-0715.[39] However, the (003) and (006) diffraction peaks show a slight shift toward higher 2θ values, which is attributed to the contraction of interlayer spacing induced by water molecules, anions, or other interlayer species.[40] Similar shifts have been reported for CTAB-assisted synthesis of $Ni(OH)_2$.[39,41] Figure 1g compares the XRD patterns of r-$NiCo_2O_4$, $Ni(OH)_2$-3, and r-$NiCo_2O_4$/$Ni(OH)_2$-3 composite loaded onto the carbon cloth. The composite exhibits the characteristic diffraction peaks of both $Ni(OH)_2$ and $NiCo_2O_4$, confirming the successful synthesis of the high-purity r-$NiCo_2O_4$/$Ni(OH)_2$-3 material.[42]

X-ray photoelectron spectroscopy (XPS) was employed to determine the elemental composition of r-$NiCo_2O_4$ and r-$NiCo_2O_4$/$Ni(OH)_2$-3 grown on the carbon cloth. As presented in Figure 1h, the growth of $Ni(OH)_2$-3 on the surface of r-$NiCo_2O_4$ partially shields the signals from the $NiCo_2O_4$. Consequently, the intensity of the Co 2p signals in the r-$NiCo_2O_4$/$Ni(OH)_2$-3 composite is noticeably attenuated, which further confirms the well-aligned nanostructure.[23] In the Ni 2p spectrum of r-$NiCo_2O_4$ (Figure 1i), two main peaks appear at 854.81 eV (Ni $2p_{3/2}$) and 872.51 eV (Ni $2p_{1/2}$), suggesting that Ni exists in mixed-valence states of Ni^{2+} and Ni^{3+}.[43] Specifically, the deconvoluted peaks at 855.98/873.42 eV are characteristic of Ni^{2+}, while those at 857.8/875.11 eV correspond to Ni^{3+}.[28] Similarly, the Co 2p spectrum (Figure 1j) exhibits characteristic doublet peaks. The deconvoluted peaks at 780.74/795.75 eV and 779.5/794.5 eV are assigned to Co^{2+} and Co^{3+}, respectively.[28,44] The O 1s photoemission in Figure 1k can be deconvoluted into three characteristic peaks, corresponding to metal−oxygen bonds (O1 at 529.35 eV), undercoordinated oxygen (O2 at 530.85 eV), and adsorbed water molecules (O3 at 532.68 eV), respectively.[45−47] Furthermore, when r-$NiCo_2O_4$ is composited with $Ni(OH)_2$-3, the fitted Ni 2p signal in Figure 1l also reveals the coexistence of two nickel valence states. The mixed-valence systems involving Ni^{2+}/Ni^{3+} and Co^{2+}/Co^{3+} can facilitate rapid charge transfer in the r-$NiCo_2O_4$/$Ni(OH)_2$-3 composite electrode, thereby enhancing electrochemical kinetics.[23,35]

Figure 2a−d present the SEM images of various $Ni(OH)_2$ samples, demonstrating that the morphology evolves significantly as a function of precursor concentration. The $Ni(OH)_2$-1 (low-concentration group) exhibits sparse growth on the carbon cloth, displaying sheet-like structures. This limited yield stems from an inadequate driving force at low precursor concentrations.[37] Increasing the concentration initially results in irregularly distributed thick sheets with moss-like structures ($Ni(OH)_2$-2), eventually transitioning to predominantly moss-like morphologies with high porosity in $Ni(OH)_2$-3 and $Ni(OH)_2$-4. This morphological shift is accompanied by an upward trend in mass loading, confirming that high precursor concentrations promote $Ni(OH)_2$ growth. The formation of the porous structure is closely related to CTAB. As a cationic surfactant, CTAB interacts with the OH^- in precursor solutions through electrostatic attraction to slow the reaction kinetics between the OH^- and Ni^{2+}, thereby suppressing the agglomeration of $Ni(OH)_2$. Furthermore, an increased CTAB concentration can promote the lateral growth of $Ni(OH)_2$ to yield a porous network.[48,49] We also performed the BET analysis for the four $Ni(OH)_2$ samples. As shown in Figure S2, the specific surface area exhibits a progressive upward trend from $Ni(OH)_2$-1 to $Ni(OH)_2$-4, which correlates well with the morphological evolution (gradual increase in porosity) observed in SEM images. Such an increase in the surface area can provide more active sites for the reaction, as confirmed by electrochemical active surface area (ECSA) measurements (Figure S3). Figure 2e−h display the SEM images of $Ni(OH)_2$ grown on r-$NiCo_2O_4$, revealing that the presence of r-$NiCo_2O_4$ results in more uniform $Ni(OH)_2$ growth and higher mass loading compared to growth on the carbon cloth. This phenomenon can be attributed to the surface of r-$NiCo_2O_4$ serving as active sites for the heterogeneous nucleation of $Ni(OH)_2$.[28] Specifically, regarding the surface morphology of the composite materials, $Ni(OH)_2$-1 forms uniform nanosheets, while $Ni(OH)_2$-2 consists of thinner nanosheets decorated with needlelike nanostructures at their edges. As for $Ni(OH)_2$-3, it transitions into a moss-like framework composed of continuous $Ni(OH)_2$, which can effectively boost reaction active sites, as discussed above. However, $Ni(OH)_2$-4 (high-concentration group) suffers from overgrowth-induced particle agglomeration.

Transmission electron microscopy (TEM) coupled with energy-dispersive X-ray spectroscopy (EDS) was used to further investigate the nanostructure of the r-$NiCo_2O_4$/$Ni(OH)_2$-3 composite, as shown in Figure 2i−l. The TEM images reveal that the $NiCo_2O_4$ nanorods, which are composed of numerous nanoparticles, are fully covered by $Ni(OH)_2$, resulting in a well-defined core−shell architecture. This structure is further corroborated by EDS elemental mapping. The overlapping signals of Ni and Co delineate the $NiCo_2O_4$ nanorod core, whereas the broader, dense distribution of Ni extending beyond the core confirms the presence of the $Ni(OH)_2$ shell. Distinct from other reported composite structures,[23,27] this needlelike insertion of $NiCo_2O_4$ into $Ni(OH)_2$ has significant impacts on the electrochemical properties and structural stability, as discussed later. To investigate the impact of the secondary hydrothermal treatment on the r-$NiCo_2O_4$ scaffold, the TEM and EDS mapping images of the pristine material (Figure S4) are compared with those of the composite. Based on the distribution of Co, which serves as a unique tracer for the r-$NiCo_2O_4$, it is evident that the rod-like morphology is well preserved and maintains intimate contact with $Ni(OH)_2$. However, the nanorods exhibit reduced lengths, which can be attributed to partial dissolution during the secondary hydrothermal treatment. This phenomenon is further verified by a control experiment where the r-$NiCo_2O_4$ was treated under the same hydrothermal conditions for the composite synthesis but without $Ni(NO_3)_2 \cdot 6H_2O$. The SEM images (Figure S5) of the resulting r-$NiCo_2O_4$ provide compelling evidence that the nanorod structure remains stable while showing a decrease in length, though the reaction environment is not completely identical. Furthermore, we conducted high-resolution TEM analysis (Figure S6) for both the pristine r-$NiCo_2O_4$ and the r-$NiCo_2O_4$/$Ni(OH)_2$-3. The r-$NiCo_2O_4$ exhibits well-defined lattice fringes with a spacing of 0.25 nm, indexed to the (311) plane. In the composite, a distinct heterointerface (indicated by the dashed line) is observed between the r-$NiCo_2O_4$ and $Ni(OH)_2$. The lattice fringes in the upper-right region remain unchanged (0.25 nm), suggesting that the r-$NiCo_2O_4$ maintains its original crystal structure after the secondary hydrothermal treatment. The preserved crystal structure is consistent with the XRD results (Figure 1g). Meanwhile, the (101) plane of $Ni(OH)_2$ is identified in the neighboring region with a lattice spacing of 0.26 nm.

https://doi.org/10.1021/acsami.6c02790
ACS Appl. Mater. Interfaces 2026, 18, 32546−32556

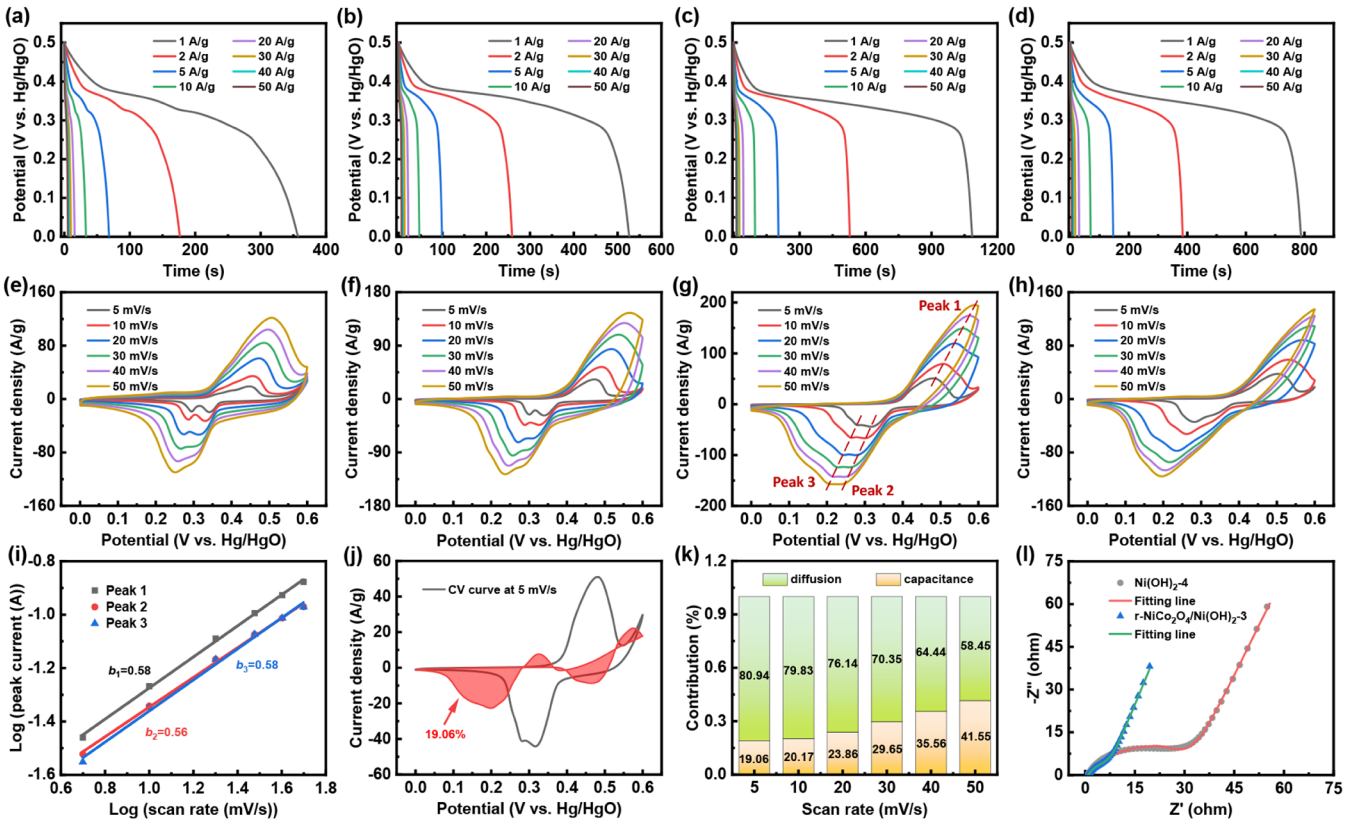


Figure 3. (a–d) Galvanostatic discharge and (e–h) CV curves of the r-$NiCo_2O_4$/$Ni(OH)_2$-1, r-$NiCo_2O_4$/$Ni(OH)_2$-2, r-$NiCo_2O_4$/$Ni(OH)_2$-3, and r-$NiCo_2O_4$/$Ni(OH)_2$-4 electrode, where (a) to (d) and (e) to (h) correspond to increasing precursor concentrations for $Ni(OH)_2$ synthesis. (i) Plots of Log(i) versus Log(v) for the $NiCo_2O_4$/$Ni(OH)_2$-3 electrode. (j) CV curve with capacitive contribution (shaded in red) of the r-$NiCo_2O_4$/$Ni(OH)_2$-3 electrode at a scan rate of 5 mV/s. (k) Normalized contribution ratios of capacitive and diffusion-controlled behaviors of the r-$NiCo_2O_4$/$Ni(OH)_2$-3 electrode at varying scan rates. (l) Nyquist plots of the $Ni(OH)_2$-4 and r-$NiCo_2O_4$/$Ni(OH)_2$-3 electrode.

2.2. Electrochemical Behavior Analysis

The electrochemical properties of the $Ni(OH)_2$-4 electrode measured in a standard three-electrode configuration are presented in Figure S7. The cyclic voltammetry (CV) curves in Figure S7a exhibit a pair of redox peaks, indicating that $Ni(OH)_2$ undergoes reversible Faradaic reactions during the scanning process. These peaks correspond to the valence transition of nickel species, which can be described by the following eq 1.[42]

$$Ni(OH)_2 + OH^- \rightleftharpoons NiOOH + H_2O + e^- \quad (1)$$

As scan rates increase, the oxidation and reduction peaks shift toward higher and lower potentials, respectively. This phenomenon stems from the kinetic mismatch between OH^- diffusion and electron transfer, leading to pronounced electrochemical polarization.[37,43] The GCD measurements (Figure S7b) show that the electrode delivers a specific capacitance of 1045.37 F/g (145.19 mAh/g) at 1 A/g. However, with the current density gradually increasing, the specific capacitance systematically decreases, as illustrated in Figure S7c. For example, when the current density reaches 50 A/g, the capacitance retention drops to merely 1.34%. The unsatisfactory rate capability also stems primarily from the poor conductivity and sluggish ion diffusion kinetics.[50]

To address the aforementioned limitations, the moss-like $Ni(OH)_2$ was integrated with three types of $NiCo_2O_4$ featuring distinct morphologies. We first characterized the electrochemical behavior of the three $NiCo_2O_4$ electrodes. Figure S8a–c present their CV curves over a scan rate range of 5–50 mV/s. All electrodes exhibit a pair of well-defined redox peaks, indicating the pseudocapacitive characteristics of $NiCo_2O_4$. The corresponding Faradaic reactions can be expressed by eqs 2 and 3.[28,35]

$$NiCo_2O_4 + H_2O + OH^- \rightleftharpoons NiOOH + 2CoOOH + e^- \quad (2)$$

$$CoOOH + OH^- \rightleftharpoons CoO_2 + H_2O + e^- \quad (3)$$

The GCD measurements (Figure S9a–c) reveal limited specific capacitances for the three $NiCo_2O_4$ electrodes, with s-$NiCo_2O_4$, sr-$NiCo_2O_4$, and r-$NiCo_2O_4$ yielding 98.00, 165.38, and 193.82 F/g (13.61, 22.97, and 26.92 mAh/g) at 1 A/g, respectively. However, the three $NiCo_2O_4$ electrodes exhibit exceptional rate capabilities. As shown in Figure S9d, even at 50 A/g, they maintain capacitance retention rates of 68.41% (s-$NiCo_2O_4$), 71.96% (sr-$NiCo_2O_4$), and 77.38% (r-$NiCo_2O_4$) relative to their initial values.

Next, the capacitive performance of various $NiCo_2O_4$/$Ni(OH)_2$ composite electrodes was investigated. The GCD analysis (Figure S10a–e) reveals that the s-$NiCo_2O_4$/$Ni(OH)_2$ composites yield marginal gains in specific capacitance, but exhibit enhanced rate capability over pristine $Ni(OH)_2$. Similar trends are observed for the sr-$NiCo_2O_4$/$Ni(OH)_2$ composites (Figure S11a–e), though they exhibit a larger improvement in specific capacitance compared with the s-$NiCo_2O_4$-based composites. For example, the sr-$NiCo_2O_4$/$Ni(OH)_2$-3 electrode delivers a specific capacitance of 1391.4 F/g (193.25

https://doi.org/10.1021/acsami.6c02790
ACS Appl. Mater. Interfaces 2026, 18, 32546–32556

mAh/g) at 1 A/g and a capacitance retention of 33.71% at 50 A/g. In contrast, r-$NiCo_2O_4$/$Ni(OH)_2$ composites, particularly the r-$NiCo_2O_4$/$Ni(OH)_2$-3 electrode, demonstrate a significant enhancement in both specific capacitance (2170.22 F/g at 1 A/g) and rate capability (82.3% at 20 A/g and 59.16% at 50 A/g), as shown in Figure 3a−d and S12. This rate capability is well-suited to accommodate the high-power output characteristic of solar energy. We also conducted the ECSA measurement for $Ni(OH)_2$-3 grown on the three different $NiCo_2O_4$ scaffolds. As shown in Figure S13, the r-$NiCo_2O_4$/$Ni(OH)_2$-3 composites exhibit an ECSA value of 617.00 cm^2, which is significantly higher than that of the s-$NiCo_2O_4$/$Ni(OH)_2$-3 (503.75 cm^2) and sr-$NiCo_2O_4$/$Ni(OH)_2$-3 (547.25 cm^2) composites. The superior electrochemical performance of r-$NiCo_2O_4$/$Ni(OH)_2$ composites stems from the high surface area of r-$NiCo_2O_4$ (Figure 1d and e), which increases the contact area with $Ni(OH)_2$, accelerating electron transport and enabling a more homogeneous distribution of the $Ni(OH)_2$. Additionally, the r-$NiCo_2O_4$ itself outperforms other morphologies in terms of capacitance and rate performance (Figure S9d), further enhancing the overall electrochemical properties of the composite.

The GCD curves also reveal the influence of the $Ni(OH)_2$ nanostructure on the capacitive performance. Among the samples, r-$NiCo_2O_4$/$Ni(OH)_2$-3, synthesized at an optimal precursor concentration, exhibits the highest specific capacitance. This is primarily attributed to its moss-like structure, which generates high specific surface areas, thereby providing abundant active sites.[38] Conversely, both insufficient and excessive precursor concentrations for $Ni(OH)_2$ synthesis result in reduced specific surface areas (as confirmed in Figure 2e−h), decreasing the capacitance. Nevertheless, all $Ni(OH)_2$ prepared via hydrothermal routes in the presence of CTAB demonstrates continuous and uniform growth over the $NiCo_2O_4$ framework, ensuring high material utilization for energy storage. Figure S14 shows the ECSA measurement for the r-$NiCo_2O_4$/$Ni(OH)_2$-n (n = 1, 2, 3, 4) electrodes. Among these, the r-$NiCo_2O_4$/$Ni(OH)_2$-3 electrode demonstrates the largest ECSA value, suggesting the highest density of electrochemically accessible active sites.[51] It is worth mentioning that the improved electrochemical performance of the composite electrode, particularly its rate capability, plays a crucial role in constructing high-performance photorechargeable devices. This is because photovoltaic modules typically generate high photocurrent densities; for instance, the PERC solar cell discussed later exhibits a short-circuit current density of 16 mA/cm.[2]

Figure 3e−h display the CV curves of various $NiCo_2O_4$/$Ni(OH)_2$ composite electrodes, revealing multiple redox peaks that are associated with the Faradaic redox reactions of both $Ni(OH)_2$ and $NiCo_2O_4$ within the composite.[52] To further elucidate the electrochemical charge-storage mechanism of the r-$NiCo_2O_4$/$Ni(OH)_2$-3 electrode, the relationship between the peak current and the scan rate in the CV curves was analyzed, following the power-law expression (eqs 4 and 5).[53]

$$i = a \times v^b \tag{4}$$

or

$$\log(i) = \log(a) + b\log(v) \tag{5}$$

where i represents the peak current (A), v is the scan rate (mV/s), and a and b are adjustable parameters.[54] The charge-storage mechanism is dictated by the parameter b, where the b-value of 0.5 and 1 correspond to Faradaic diffusion-controlled and non-Faradaic capacitive processes, respectively. Figure 3i presents the plots of Log(i) versus Log(v), from which the b-values for peaks 1−3 (as labeled in Figure 3g) are calculated to be 0.58, 0.56, and 0.58, respectively. These values, being closer to 0.5 than to 1.0, indicate a predominantly diffusion-controlled process for the r-$NiCo_2O_4$/$Ni(OH)_2$-3 composites, which aligns with the later quantitative analysis showing a high diffusive contribution even at 50 mV/s. Equations 6 and 7 were employed to further quantitatively distinguish the relative contributions of the two storage mechanisms.[55]

$$i(V) = k_1 v + k_2 v^{1/2} \tag{6}$$

or

$$\frac{i}{v^{1/2}} = k_1 v^{1/2} + k_2 \tag{7}$$

where $k_1 v$ and $k_2 v^{1/2}$ correspond to the contributions of capacitive-controlled and diffusion-controlled processes to the total capacitance, respectively. The values of k_1 and k_2 were obtained by fitting the curves according to eq 7. Figure 3j shows that the capacitive contribution accounts for 19.06% at a scan rate of 5 mV/s. With the scan rate increasing, the capacitive contribution exhibits a monotonic rise, while the diffusion-controlled fraction correspondingly decreases, as illustrated in Figure 3k. Notably, even at a high scan rate of 50 mV/s, the diffusive contribution persists at 58.45%, indicating its predominant role in the overall charge-storage process. This observation is closely related to the structural characteristics of the composite. The porous architecture of the r-$NiCo_2O_4$/$Ni(OH)_2$-3 composite significantly expands the electrode−electrolyte contact area, while the continuous $Ni(OH)_2$ loading facilitates efficient ion diffusion across the entire composite framework. Collectively, these features synergistically enhance Faradaic reaction kinetics, thereby maintaining the dominance of the diffusion-controlled energy storage process.[28]

Figure 3l displays the electrochemical impedance spectroscopy (EIS) plots for the r-$NiCo_2O_4$/$Ni(OH)_2$-3 and $Ni(OH)_2$-4 electrode. The experimental data (symbols) are accurately fitted with equivalent circuit models (solid curves). In the high-frequency region, the intercept on the x-axis and the semicircle diameter represent the series resistance (R_s) and charge-transfer resistance (R_{ct}), respectively.[56,57] The $Ni(OH)_2$-4 electrode exhibits an R_s of 0.84 Ω and an R_{ct} of 22.15 Ω. Remarkably, the r-$NiCo_2O_4$/$Ni(OH)_2$-3 composite shows a significantly smaller semicircle, yielding a much lower R_{ct} of 10.61 Ω. In the low-frequency range, the steeper slope of the inclined line for the composite electrode indicates a reduced Warburg impedance (Z_W), signifying faster ion diffusion.[58,59] These results confirm that the rational coupling of $NiCo_2O_4$ and $Ni(OH)_2$ optimizes charge-transfer kinetics, facilitating efficient ion/electron transport within the composite electrode.[37,42] The enhanced kinetics are attributed not only to the uniquely engineered nanostructure but also to the heterojunction structure between $NiCo_2O_4$ and $Ni(OH)_2$, which facilitates electron transport.[60,61]

2.3. Characterization of Supercapacitor Performance

Activated carbon (AC) was paired with the r-$NiCo_2O_4$/$Ni(OH)_2$-3 composite to assemble asymmetric supercapacitors (ASCs). The electrochemical characteristics of the AC electrode, measured in a three-electrode configuration. The

https://doi.org/10.1021/acsami.6c02790
ACS Appl. Mater. Interfaces 2026, 18, 32546−32556

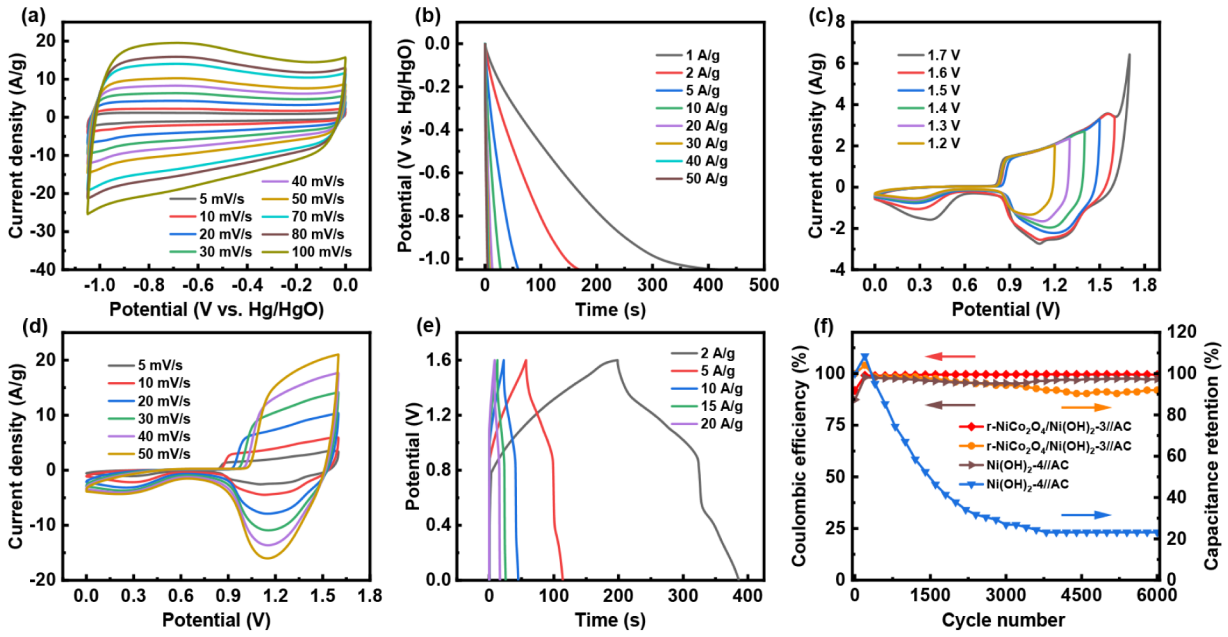


Figure 4. (a) CV curves and (b) galvanostatic discharge curves of the AC electrode. (c) CV responses of the r-$NiCo_2O_4$/$Ni(OH)_2$-3//AC ASC measured at various potential windows. (d) CV curves and (e) GCD curves of the r-$NiCo_2O_4$/$Ni(OH)_2$-3//AC ASC at varying scan rates and current densities, respectively. (f) Long-term cycling performance of the r-$NiCo_2O_4$/$Ni(OH)_2$-3//AC and $Ni(OH)_2$-4//AC ASC at 2 A/g.

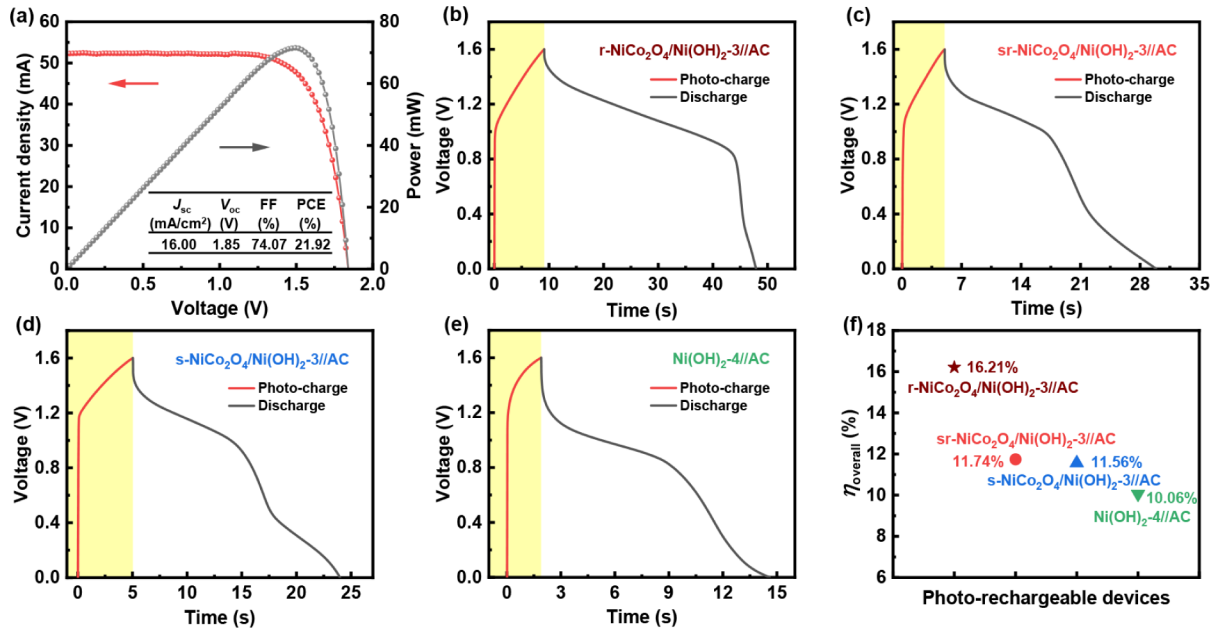


Figure 5. (a) Current−voltage and power-voltage plots of the PERC solar cell. (b−e) Photocharge and galvanostatic discharge (at 5 A/g) profiles of photorechargeable devices integrating various ASCs with the PERC solar cell. (f) Overall efficiency of four photorechargeable supercapacitors.

CV curves (Figure 4a) exhibit a quasi-rectangular shape, indicative of electric double-layer capacitive (EDLC) behavior. As shown in Figure 4b, the AC electrode delivers a specific capacitance of 398.19 F/g at 1 A/g, and maintains a retention of 54.02% even as the current density scales to 50 A/g. Based on these parameters, the optimal negative-to-positive (N/P) mass ratio was determined (detailed in the Supporting Information). The electrochemical performance of the assembled ASC is presented in Figure 4c−e. The CV recorded within various potential windows (Figure 4c) confirms an optimal operating potential of 0−1.6 V, as evident oxygen evolution occurs when the potential exceeds 1.7 V. Figure 4d illustrates the CV curves within the defined safe potential window at scan rates from 5 to 50 mV/s. These profiles exhibit characteristic redox features consistent with previously reported literature.[36] Notably, the CV curves remain largely undistorted with increasing scan rates, suggesting excellent rate capability. As shown in Figure 4e, the ASC exhibits a specific capacitance of 234.25 F/g at 2 A/g. Even at current densities of 5, 10, and 20 A/g, the device sustains a relatively high capacitance.

To assess the long-term cycling durability, both the r-$NiCo_2O_4$/$Ni(OH)_2$-3//AC and $Ni(OH)_2$//AC ASCs were tested at a constant temperature of 25 °C via GCD cycling at 2

https://doi.org/10.1021/acsami.6c02790
ACS Appl. Mater. Interfaces 2026, 18, 32546−32556

A/g for 6000 cycles. As shown in Figure 4f, the r-$NiCo_2O_4$/$Ni(OH)_2$-3//AC ASC retains 91.94% of its initial capacitance, a performance substantially superior to that of the $Ni(OH)_2$//AC counterpart. We further characterized the electrochemical performance of the r-$NiCo_2O_4$/$Ni(OH)_2$-3 electrode after the stability test. As shown in Figure S15a, the CV curve remains largely consistent with the precycling profile, maintaining well-defined redox peaks despite a marginal reduction in current response. Similarly, the GCD curve (Figure S15b) exhibits a slight decrease in discharge duration, the extent of which aligns well with the capacitance decay observed in the stability test. The EIS data (Figure S15c) exhibit a slight increase in R_{ct} (from 0.55 Ω to 0.69 Ω) after the long-term cycling, indicating that the charge-transfer kinetics are largely preserved. Figure S16 compares the SEM images of the r-$NiCo_2O_4$/$Ni(OH)_2$-3 electrode before and after the stability test, demonstrating that the composite maintains its moss-like morphology without significant collapse or detachment, while undergoing a slight evolution toward more distinct nanosheet-structured features. Although the marginal morphological evolution and R_{ct} increment can collectively contribute to the modest capacitance decay, the cycling stability of the r-$NiCo_2O_4$/$Ni(OH)_2$-3//AC ASC outperforms many previously reported composite-based ASCs, as summarized in Table S1. This exceptional durability can be attributed to the microstructural advantages of the composite. Specifically, the $NiCo_2O_4$ nanorods, uniformly embedded within the continuous $Ni(OH)_2$, act as a rigid backbone to buffer volume expansion. This structure effectively mitigates active material pulverization during charge−discharge processes, while homogenizing cyclic stress to preclude localized structural failure.[62]

2.4. Evaluation of Photorechargeable Devices

To further explore the solar energy storage capabilities of the as-prepared ASCs, photorechargeable devices were constructed by coupling four ASCs (r-$NiCo_2O_4$/$Ni(OH)_2$-3//AC, sr-$NiCo_2O_4$/$Ni(OH)_2$-3//AC, s-$NiCo_2O_4$/$Ni(OH)_2$-3//AC, and $Ni(OH)_2$-4//AC) with PERC solar cells for performance characterization. As for the photovoltaic module, three PERC solar cells with a total effective area of 3.27 cm^2 were connected in series. As illustrated in Figure 5a, the photovoltaic module exhibits an open-circuit voltage (V_{oc}) of 1.85 V, a short-circuit current density (J_{sc}) of 16 mA/cm^2, and a fill factor (FF) of 74.07%, achieving a power conversion efficiency (PCE) of 21.92% at 1.49 V. Considering both the photovoltaic output characteristics and the electrochemical behaviors of the ASCs, a photocharging cutoff voltage of 1.6 V was selected.

Figure 5b−e illustrate the photocharge and dark discharge curves of the four photorechargeable supercapacitors. The photocharge curves reveal that the r-$NiCo_2O_4$/$Ni(OH)_2$-3-based device exhibits a lower inflection voltage (approximately 1 V), whereas the $Ni(OH)_2$-based counterpart shows a higher value (around 1.1 V). Our previous research has demonstrated that the inflection voltage signifies the transition from EDLC-dominant to pseudocapacitive-dominant storage behavior; notably, minimizing the voltage mismatch between this inflection point and the maximum power point (MPP) of photovoltaic module can enhance the overall efficiency of photorechargeable devices.[63] Given that all devices in this study store energy via Ni-based redox reactions, the elevated inflection voltage observed in the $Ni(OH)_2$-based device, which brings it closer to the MPP voltage, is primarily attributed to severe polarization at high current densities. The presence of severe polarization in the pristine $Ni(OH)_2$ is supported by the EIS data (Figure 3l), where its higher R_{ct} relative to the composite indicates significantly more sluggish charge-transfer kinetics. Consequently, although the $Ni(OH)_2$-based device allows the photovoltaic module to operate at a higher apparent efficiency, a substantial fraction of the converted energy is lost as heat, resulting in lower actual energy storage. Additionally, the discharge curves confirm that the r-$NiCo_2O_4$/$Ni(OH)_2$-3 device achieves the highest specific capacitance. The capacitance trends across the four devices match those observed in their respective electrode materials (Figures 3, S7, and S10−11), further emphasizing the critical impact of material design on the performance of photorechargeable devices. The overall solar-to-electrochemical energy efficiency ($\eta_{overall}$) of the four photorechargeable supercapacitors was calculated using the following eq 8[4,9]

$$\eta_{overall} = \frac{I_{dischage} \int V_{dischage} dt_2}{SP_{light} t_1} \quad (8)$$

where $I_{discharge}$ denotes the discharge current of the energy storage module, $V_{discharge}$ represents the voltage during the discharge process, and t_2 is the discharge time. Meanwhile, S refers to the area of the light source, P_{light} corresponds to the incident light power density, and t_1 is the photocharge time. As shown in Figure 5f, the r-$NiCo_2O_4$/$Ni(OH)_2$-3-based device achieves the highest overall efficiency of 16.21%. The significantly lower efficiency of the $Ni(OH)_2$-based device also confirms that the pristine $Ni(OH)_2$ electrode materials induce severe energy losses during the energy storage process. These results in Figure 5 demonstrate that the device integrating r-$NiCo_2O_4$/$Ni(OH)_2$-3//AC ASC with PERC solar cell exhibit exceptional solar-to-storage capability, making it a promising candidate for powering miniaturized electronics.[21,64,65] To further demonstrate its practical utility, a LED lighting experiment was conducted. After being photocharged under simulated sunlight, two devices connected in series successfully power a commercial LED with stable light emission, as shown in Figure S17. This demonstration validates the feasibility of the as-fabricated devices to harvest and store solar energy for on-demand power supply.

3. CONCLUSION

This work significantly enhances the capacitive performance of $NiCo_2O_4$/$Ni(OH)_2$ composite electrodes through rational nanostructure engineering, facilitating the development of high-performance photorechargeable device. It is found that $NiCo_2O_4$ nanorods, compared to nanosheet or mixed nanorod-nanosheet morphologies, possess a larger specific surface area that effectively increases the contact interface and mass loading of $Ni(OH)_2$; furthermore, their superior intrinsic capacitance and rate capability effectively support the enhanced electrochemical properties of the resulting composite electrodes. Integrating the $NiCo_2O_4$ nanorods with $Ni(OH)_2$ across varying precursor concentrations reveals that an optimal concentration induces a continuous and high-surface-area $Ni(OH)_2$ growth on the nanorod surfaces, with the nanorods homogeneously embedded within the $Ni(OH)_2$. This unique nanostructure not only increases electrochemically active sites, but also greatly promotes rapid electron/ion transport and enhances structural stability. Consequently, the resulting ASCs exhibit dramatic improvements in specific capacitance, rate performance, and cycling stability. Notably, the enhanced rate

https://doi.org/10.1021/acsami.6c02790
ACS Appl. Mater. Interfaces 2026, 18, 32546−32556

performance greatly accommodates the high-current characteristics of photovoltaic modules, ensuring the effective storage of converted electrical energy. By integrating the r-$NiCo_2O_4$/$Ni(OH)_2$-3//AC ASC with PERC solar cells, the as-fabricated device achieves a solar-to-electrochemical energy efficiency of 16.21%, paving the way for the development of future solar-driven self-charging electronics.

4. EXPERIMENTAL SECTION

4.1. Synthesis of $NiCo_2O_4$ with Various Morphologies

$NiCo_2O_4$ samples with different morphologies were synthesized via a hydrothermal method followed by calcination. For the synthesis of s-$NiCo_2O_4$, 0.45 mmol $NiCl_2{\cdot}6H_2O$, 0.9 mmol $Co(NO_3)_2{\cdot}6H_2O$, 2.7 mmol NH_4F, and 4.5 mmol hexamethylenetetramine (HMTA) were dissolved in 60 mL deionized water. The mixture was transferred to a 100 mL PTFE-lined autoclave and stirred for 10 min. The pretreated carbon cloth (10 mm × 15 mm) was then fully immersed in the resulting homogeneous solution, followed by being maintained at 120 °C for 6 h. sr-$NiCo_2O_4$ was prepared using a similar procedure but with 0.5 mmol $NiCl_2{\cdot}6H_2O$, 1 mmol $CoCl_2{\cdot}6H_2O$, 3 mmol NH_4F, and 7.5 mmol urea as precursors, reacting at 120 °C for 2 h. For r-$NiCo_2O_4$, 0.6 mmol $Ni(NO_3)_2{\cdot}6H_2O$, 1.2 mmol $Co(NO_3)_2{\cdot}6H_2O$, and 7.2 mmol urea were dissolved in a 60 mL mixed solvent (water: ethanol = 1:1, v/v) and heated at 100 °C for 6 h. After cooling to room temperature, the resulting precursor-loaded carbon cloths were rinsed thoroughly with deionized water and ethanol, and dried at 60 °C. Finally, the samples were calcined at 350 °C for 2 h (ramping rate: 5 °C/min) to yield the final products.

4.2. Synthesis of Different $NiCo_2O_4$/$Ni(OH)_2$ Composites

The $NiCo_2O_4$/$Ni(OH)_2$ composites were prepared through a secondary hydrothermal process. In a typical synthesis, 0.5 mmol $Ni(NO_3)_2{\cdot}6H_2O$, 3 mmol urea, and 0.25 mmol hexadecyltrimethylammonium bromide (CTAB) were dissolved in 60 mL deionized water. The as-prepared r-$NiCo_2O_4$ substrate was immersed in this solution, which was then maintained at 120 °C for 6 h in a 100 mL PTFE-lined autoclave. The obtained samples were washed, dried at 60 °C, obtaining r-$NiCo_2O_4$/$Ni(OH)_2$-1 composite electrodes. Then, the concentrations of all precursors were scaled by factors of 2, 3, and 4 to yield r-$NiCo_2O_4$/$Ni(OH)_2$-n, where n (n = 2, 3, 4) represents the corresponding concentration fold change relative to the initial formulation. Following the same protocol, composites using s-$NiCo_2O_4$ and sr-$NiCo_2O_4$ as substrates were prepared and denoted as s-$NiCo_2O_4$/$Ni(OH)_2$-n and sr-$NiCo_2O_4$/$Ni(OH)_2$-n, respectively. Similarly, pure $Ni(OH)_2$-n electrodes were also synthesized on bare carbon cloths under identical conditions. Experimental details regarding characterization methods are provided in the Supporting Information.

■ ASSOCIATED CONTENT

Supporting Information

The Supporting Information is available free of charge at https://pubs.acs.org/doi/10.1021/acsami.6c02790.

Characterization methods, SEM images, EDS mapping, TEM images, BET specific surface area, ECSA measurement, CV curves, GCD curves, EIS spectra, and cycling stability performance (PDF)

■ AUTHOR INFORMATION

Corresponding Authors

Meicheng Li − *State Key Laboratory of Alternate Electrical Power System with Renewable Energy, School of New Energy, North China Electric Power University, Beijing 10026, China*; orcid.org/0000-0002-0731-741X; Email: mcli@ncepu.edu.cn

Xin Sun − *State Key Laboratory of Alternate Electrical Power System with Renewable Energy, School of New Energy, North China Electric Power University, Beijing 10026, China*; Email: xsun@ncepu.edu.cn

Authors

Changhua Mi − *State Key Laboratory of Alternate Electrical Power System with Renewable Energy, School of New Energy, North China Electric Power University, Beijing 10026, China*

Haowei Yu − *State Key Laboratory of Alternate Electrical Power System with Renewable Energy, School of New Energy, North China Electric Power University, Beijing 10026, China*

Yudong Han − *State Key Laboratory of Alternate Electrical Power System with Renewable Energy, School of New Energy, North China Electric Power University, Beijing 10026, China*

Yiqi Wang − *State Key Laboratory of Alternate Electrical Power System with Renewable Energy, School of New Energy, North China Electric Power University, Beijing 10026, China*

Cewen Xin − *State Key Laboratory of Alternate Electrical Power System with Renewable Energy, School of New Energy, North China Electric Power University, Beijing 10026, China*

Jiahao Yang − *State Key Laboratory of Alternate Electrical Power System with Renewable Energy, School of New Energy, North China Electric Power University, Beijing 10026, China*

Jingang Guo − *State Key Laboratory of Alternate Electrical Power System with Renewable Energy, School of New Energy, North China Electric Power University, Beijing 10026, China*

Jianan Gu − *State Key Laboratory of Alternate Electrical Power System with Renewable Energy, School of New Energy, North China Electric Power University, Beijing 10026, China*; orcid.org/0000-0003-3914-5760

Yanlong Lv − *State Key Laboratory of Alternate Electrical Power System with Renewable Energy, School of New Energy, North China Electric Power University, Beijing 10026, China*

Yanhong Wang − *State Key Laboratory of Alternate Electrical Power System with Renewable Energy, School of New Energy, North China Electric Power University, Beijing 10026, China*

Complete contact information is available at: https://pubs.acs.org/10.1021/acsami.6c02790

Author Contributions

The manuscript was written through contributions of all authors. All authors have given approval to the final version of the manuscript.

Notes

The authors declare no competing financial interest.

■ ACKNOWLEDGMENTS

This work was partially supported by the Beijing Natural Science Foundation (26JL001), the National Natural Science Foundation of China (52302250), the Hebei Natural Science Foundation (B2024502013), the Special Project for Beijing-Tianjin-Hebei Basic Research Cooperation (B2024202087),

the 2022 Strategic Research Key Project of the Science and Technology Commission of the Ministry of Education, the China Postdoctoral Science Foundation (2022M721129), the Fundamental Research Funds for the Central Universities (2025MS046 and 2025JC006), and the NCEPU "Double First-Class" Program.

REFERENCES

(1) Senthil, R. A.; Min, A.; Theerthagiri, J.; Kim, G.-A.; Choi, H. C.; Choi, M. Y. Insights on Ni-based layered double hydroxides for electrochemical supercapacitors: Underlying aspects in rational design and structural evolution. *J. Energy Storage* **2023**, *72*, 108305.

(2) Iqbal, M. Z.; Faisal, M. M.; Ali, S. R. Integration of supercapacitors and batteries towards high-performance hybrid energy storage devices. *Int. J. Energy Res.* **2021**, *45* (2), 1449−1479.

(3) Bi, J.; Li, S.; Liu, D.; Li, B.; Yang, K.; Xu, M.; Fu, C.; Zhao, Y.; Zhang, W. Highly integrated perovskite solar cells-based photo-rechargeable system with excellent photoelectric conversion and energy storage ability. *Energy Environ. Mater.* **2024**, *7* (5), No. e12728.

(4) Zhang, X.; Jiao, L.; Guo, W.; Xiao, Z.; Zhou, E.; Tan, Y.-X.; Feng, Y.; Yuan, D.; Wang, Y. A coupled organic solar battery with 12.1% efficiency. *J. Am. Chem. Soc.* **2025**, *147* (25), 21443−21450.

(5) Meng, H.; Pang, S.; Cui, G. Photo-supercapacitors based on third-generation solar cells. *ChemSuschem* **2019**, *12* (15), 3431−3447.

(6) Wang, Z.; Liu, R.; Wang, J.; Wang, B.; Zhu, M.; Hu, S. High energy conversion efficiency and cycle durability of solar-powered self-sustaining light-assisted rechargeable zinc−air batteries system. *Energy Storage Mater.* **2025**, *74*, 103897.

(7) Pujari, A.; Shimokawa, K.; De Volder, M. Photobatteries: Prospects and fundamental limitations. *Joule* **2025**, *9* (3), 101869.

(8) Song, Z.; Wu, J.; Tu, Y.; Sun, L.; Zhu, T.; Li, G.; Wang, X.; Du, Y.; Deng, C.; Chen, Q.; et al. Photocapacitor integrating voltage-adjustable hybrid supercapacitor and silicon solar cell generating a Joule efficiency of 86%. *Energy Environ. Sci.* **2022**, *15* (10), 4247−4258.

(9) Guo, M.; Ma, X.; Fu, J.; Chen, X.; Liu, X.; Li, Q.; Guo, W.; Lu, J. Topochemical oxidation preparation of LK-birnessite with enhanced Zn-ion storage performance for solar-powered devices. *J. Alloys Compd.* **2025**, *1022*, 179929.

(10) Yu, F.; Shen, H.; Zhang, Y.; Qiu, T.; Wang, Y.; Wang, R.; Yang, Z.; Zhang, K.; Liu, H.; Guo, C.; et al. Recent advances in integrated solar photovoltaic energy storage. *Small* **2025**, *21* (18), 2501618.

(11) Tian, Z.; Sun, Z.; Shao, Y.; Gao, L.; Huang, R.; Shao, Y.; Kaner, R. B.; Sun, J. Ultrafast rechargeable Zn micro-batteries endowing a wearable solar charging system with high overall efficiency. *Energy Environ. Sci.* **2021**, *14* (3), 1602−1611.

(12) Prishkolnik, N.; Shauloff, N.; Kanti Bhaumik, S.; Biswas, S.; Morag, A.; Jelinek, R. Photorechargeable carbon dot/thermores-ponsive polymer supercapacitor. *Small Struct* **2025**, *6* (3), 2400533.

(13) Song, W.; Zhu, Y.; Farhadi, B.; Jiang, X.; Guo, X.; Wang, S.; Zhou, C.; Li, X.; Gao, Y.; Ma, W.; et al. Multi-ion channel functional gel electrolytes enable 1.55 V open-circuit voltage and high conversion efficiency in photorechargeable zinc−air batteries. *Nano Res.* **2025**, *18* (10), 94907817.

(14) Li, X.; Xing, X.; Farhadi, B.; Zhang, H.; Zhou, C.; Guo, X.; Song, W.; Gao, Y.; Wang, K.; Chen, M.; et al. Molecule-level hybridization of MXene-Azo molecule for enhanced electrode affinity and photorechargeable supercapacitor performance. *ACS Appl. Energy Mater.* **2025**, *8* (19), 14215−14227.

(15) Shao, Y. L.; El-Kady, M. F.; Sun, J. Y.; Li, Y. G.; Zhang, Q. H.; Zhu, M. F.; Wang, H. Z.; Dunn, B.; Kaner, R. B. Design and mechanisms of asymmetric supercapacitors. *Chem. Rev.* **2018**, *118* (18), 9233−9280.

(16) Yuan, Y.; Wu, Y.; Zhang, T.; Tang, H.; Meng, L.; Zeng, Y.-J.; Zhang, Q.; Ye, Z.; Lu, J. Integration of solar cells with hierarchical CoS_x nanonets hybrid supercapacitors for self-powered photo-detection systems. *J. Power Sources* **2018**, *404*, 118−125.

(17) Kang, J.; Xue, Y.; Yang, J.; Hu, Q.; Zhang, Q.; Gu, L.; Selloni, A.; Liu, L.-M.; Guo, L. Realizing two-electron transfer in $Ni(OH)_2$ nanosheets for energy storage. *J. Am. Chem. Soc.* **2022**, *144* (20), 8969−8976.

(18) Natarajan, S.; Ulaganathan, M.; Aravindan, V. Building next-generation supercapacitors with battery type $Ni(OH)_2$. *J. Mater. Chem. A* **2021**, *9* (28), 15542−15585.

(19) Fu, M.; Zhu, Z.; Chen, W.; Yu, H.; Lv, R. Carbon cloth supported flower-like porous nickel-based electrodes boosting ion/charge transfer characteristics of flexible supercapacitors. *Carbon* **2022**, *199*, 520−528.

(20) Patil, S. A.; Jagdale, P. B.; Sfeir, A.; Pathak, M.; Royer, S.; Samal, A. K.; Rout, C. S.; Saxena, M. Flexible micro-supercapacitors with high-energy-density $Ni(OH)_2$ nanosheet: A scalable approach for enhanced volumetric performance. *J. Energy Storage* **2025**, *121*, 116526.

(21) Tan, P.; Xiao, T.; Tan, X.; Xiang, P.; Jiang, L.; Wu, D. Facile preparation of 3D porous $Ni(OH)_2$/AC−Ni as high performance binder free electrode for supercapacitors. *J. Alloys Compd.* **2016**, *656*, 714−719.

(22) Parveen, N. Morphology induced symmetrical supercapacitive performance of the 3D interconnected $Ni(OH)_2$ framework. *J. Energy Storage* **2023**, *68*, 107762.

(23) Xia, P.; Wang, Q.; Wang, Y.; Quan, W.; Jiang, D.; Chen, M. Hierarchical $NiCo_2O_4$@$Ni(OH)_2$ core-shell nanoarrays as advanced electrodes for asymmetric supercapacitors with high energy density. *J. Alloys Compd.* **2019**, *771*, 784−792.

(24) Kumar, R. $NiCo_2O_4$ nano-/microstructures as high-performance biosensors: A review. *Nano Micro Lett.* **2020**, *12* (1), 122.

(25) Wang, X.; Sun, J.; Zhao, J.; Zhou, Z.; Zhang, Q.; Wong, C.-P.; Yao, Y. All-solid-state fiber-shaped asymmetric supercapacitors with ultrahigh energy density based on porous vanadium nitride nanowires and ultrathin $Ni(OH)_2$ nanosheet wrapped $NiCo_2O_4$ nanowires arrays electrode. *J. Phys. Chem. C* **2019**, *123* (2), 985−993.

(26) Tong, H.; Yue, S.; Jin, F.; Lu, L.; Meng, Q.; Zhang, X. Honeycomb-like $NiCo_2O_4$@$Ni(OH)_2$ supported on 3D N−doped graphene/carbon nanotubes sponge as an high performance electrode for Supercapacitor. *Ceram. Int.* **2018**, *44* (3), 3113−3121.

(27) Huang, L.; Chen, D.; Ding, Y.; Wang, Z. L.; Zeng, Z.; Liu, M. Hybrid composite $Ni(OH)_2$@$NiCo_2O_4$ grown on carbon fiber paper for high-performance supercapacitors. *ACS Appl. Mater. Interfaces* **2013**, *5* (21), 11159−11162.

(28) Xu, L.; Zhang, L.; Cheng, B.; Yu, J. Rationally designed hierarchical $NiCo_2O_4$−C@$Ni(OH)_2$ core-shell nanofibers for high performance supercapacitors. *Carbon* **2019**, *152*, 652−660.

(29) Teng, Y.; Huo, Y.-Q.; Li, S.-T.; Niu, X.-M.; Fan, N.; Su, Z.-M. A zipper-like $NiCo_2O_4$/$Ni(OH)_2$ growing on multifunctional nickel foam with excellent capacitive performance. *J. Alloys Compd.* **2019**, *784*, 712−719.

(30) Chuo, H. X.; Gao, H.; Yang, Q.; Zhang, N.; Bu, W. B.; Zhang, X. T. Rationally designed hierarchical $ZnCo_2O_4$/$Ni(OH)_2$ nanostructures for high-performance pseudocapacitor electrodes. *J. Mater. Chem. A* **2014**, *2* (48), 20462−20469.

(31) Wang, Q.; Wang, X.; Xu, J.; Ouyang, X.; Hou, X.; Chen, D.; Wang, R.; Shen, G. Flexible coaxial-type fiber supercapacitor based on $NiCo_2O_4$ nanosheets electrodes. *Nano Energy* **2014**, *8*, 44−51.

(32) Jabeen, N.; Xia, Q.; Yang, M.; Xia, H. Unique core−shell nanorod arrays with polyaniline deposited into mesoporous $NiCo_2O_4$ support for high-performance supercapacitor electrodes. *ACS Appl. Mater. Interfaces* **2016**, *8* (9), 6093−6100.

(33) Wang, S.; Yang, P.; Sun, X.; Feng, L.; Jin, C.; Ren, M.; Xing, H.; Shi, J. Fabrication of the flower-like $NiCo_2O_4$@$Ni(OH)_2$/NiOOH composites supported on nickel foam by the green solvent dimethyl sulfoxide with high performance in supercapacitor and hydrogen evolution reaction. *J. Phys. Chem. Solids* **2021**, *159*, 110257.

(34) Ma, W.; He, P.; Zhou, Y.; Xie, C.; Chen, Y.; Liu, X.; Lin, S.; Zuo, P.; Zhuang, Q. $NiCo_2O_4$/hollow mesoporous carbon nanosphere hybrids enabling super-hydrophobicity, thermal insulation, and highly efficient microwave absorption. *Small* **2023**, *19* (49), 2305353.

https://doi.org/10.1021/acsami.6c02790
ACS Appl. Mater. Interfaces 2026, 18, 32546−32556

(35) Wang, B.; Cao, Y.; Chen, Y.; Wang, R.; Wang, X.; Lai, X.; Xiao, C.; Tu, J.; Ding, S. Microwave-assisted fast synthesis of hierarchical $NiCo_2O_4$ nanoflower-like supported $Ni(OH)_2$ nanoparticles with an enhanced electrocatalytic activity towards methanol oxidation. *Inorg. Chem. Front.* **2018**, *5* (1), 172−182.
(36) Chaitra, K.; Narendra, R.; Venkatesh, K.; Nagaraju, N.; Kathyayini, N. "Green" carbon with hierarchical three dimensional porous structure derived from - Pongamia pinnata seed oil extract cake and $NiCo_2O_4$-$Ni(OH)_2$/Multiwall carbon nanotubes nanocomposite as electrode materials for high performance asymmetric supercapacitor. *J. Power Sources* **2017**, *356*, 212−222.
(37) Wang, J.; Liu, Z.; Zhao, Y. Alcohol hydroxides regulate the growth of Ni-Co layered double hydroxides on carbon fiber cloth as supercapacitor electrode materials. *Electrochim. Acta* **2022**, *403*, 139645.
(38) Lu, Z.; Yang, Q.; Zhu, W.; Chang, Z.; Liu, J.; Sun, X.; Evans, D. G.; Duan, X. Hierarchical Co_3O_4@Ni-Co-O supercapacitor electrodes with ultrahigh specific capacitance per area. *Nano Res.* **2012**, *5* (5), 369−378.
(39) Wang, F. L.; Liu, X. H.; Chen, F. S.; Wan, H.; Lin, Y. F.; Zhang, N.; Ma, R. Z. Advanced supercapacitors based on α-$Ni(OH)_2$ nanoplates/graphene composite electrodes with high energy and power density. *ACS Appl. Energy Mater.* **2018**, *1* (4), 1496−1505.
(40) Kimmel, S. W.; Hopkins, B. J.; Chervin, C. N.; Skeele, N. L.; Ko, J. S.; De Block, R. H.; Long, J. W.; Parker, J. F.; Hudak, B. M.; Stroud, R. M.; et al. Capacity and phase stability of metal-substituted α-$Ni(OH)_2$ nanosheets in aqueous Ni−Zn batteries. *Mater. Adv.* **2021**, *2* (9), 3060−3074.
(41) Ren, X.; Gan, Z.; Sun, M.; Fang, Q.; Yan, Y.; Sun, Y.; Huang, J.; Cao, B.; Shen, W.; Li, Z.; et al. Colloidal synthesis of flower-like Zn doped $Ni(OH)_2$@CNTs at room-temperature for hybrid supercapacitor with high rate capability and energy density. *Electrochim. Acta* **2022**, *414*, 140208.
(42) Zhang, J.; Gao, H.; Yang, Q.; Zhang, X. T.; Zhang, M. Y.; Xu, L. L. Effect of temperature on pseudocapacitance performance of carbon fiber@$NiCo_2O_4$@$Ni(OH)_2$ core−shell nanowire array composite electrodes. *Appl. Surf. Sci.* **2015**, *356*, 167−172.
(43) Liu, L.; Hou, Y.; Gao, Y.; Yang, N.; Liu, J.; Wang, X. Co doped α-$Ni(OH)_2$ multiple-dimensional structure electrode material. *Electrochim. Acta* **2019**, *295*, 340−346.
(44) An, C.; Wang, Y.; Huang, Y.; Xu, Y.; Jiao, L.; Yuan, H. Porous $NiCo_2O_4$ nanostructures for high performance supercapacitors via a microemulsion technique. *Nano Energy* **2014**, *10*, 125−134.
(45) Nan, J.; Shi, Y.; Xiang, Z.; Wang, S.; Yang, J.; Zhang, B. Ultrathin $NiCo_2O_4$ nanosheets assembled on biomass-derived carbon microsheets with polydopamine for high-performance hybrid supercapacitors. *Electrochim. Acta* **2019**, *301*, 107−116.
(46) Sun, X.; Wang, M.; Li, H.-F.; Meng, L.; Lv, X.-J.; Li, L.; Li, M. Pristine $GaFeO_3$ photoanodes with surface charge transfer efficiency of almost unity at 1.23 V for photoelectrochemical water splitting. *Adv. Sci.* **2023**, *10* (8), 2205907.
(47) Sun, X.; Wang, M.; Geng, Q.; Chen, S.; Lv, X.; Ding, X.; Li, M. Nanostructured $AlFeO_3$ thin films as a novel photoanode for photoelectrochemical water splitting. *Nano Res.* **2024**, *17* (3), 1075−1085.
(48) Cheng, X. L.; Zhang, D. M.; Liu, X. W.; Cao, D. X.; Wang, G. L. Influence of CTAB on morphology, structure, and supercapacitance of β-$Ni(OH)_2$. *Ionics* **2015**, *21* (2), 533−540.
(49) Liang, R. F.; Wang, G. P.; Huang, X. B.; Zhu, L. W.; Li, S. W.; Yan, Y. H.; Zhong, B. H. Improving the specific capacitance of $Ni(OH)_2$-based supercapacitors by tailoring its porous structures and particle size. *Mater. Lett.* **2015**, *158*, 128−131.
(50) Nie, G.; Zhang, Z.; Liu, Y.; Wang, J.; Fu, C.; Yin, H.; Chen, J.; Zhao, L.; Pan, Z. One-pot rational deposition of coaxial double-layer MnO_2/$Ni(OH)_2$ nanosheets on carbon nanofibers for high-performance supercapacitors. *Adv. Fiber Mater.* **2022**, *4* (5), 1129−1140.
(51) Jin, X.; Feng, L.; Zhang, J.; Yuan, W.; Guo, X. Template-induced $Ni(OH)_2$ nanosheet-constructed hierarchically porous aerogel boosts superior specific capacitance and rate performance for supercapacitors. *ACS Appl. Nano Mater.* **2023**, *6* (24), 22837−22845.
(52) Yang, H.; Mu, J.; Wang, J.; Li, F.; Che, H.; Huang, Z.; Wang, Y.; Guo, Z.; Ren, L. Enhanced interfacial charge transfer via in-situ construction of integrated NiO/$NiCo_2O_4$ heterojunction coupled with carbon layer for high-performance supercapacitor and photocatalysis. *Colloids Surf., A* **2023**, *676*, 132247.
(53) Najafi, M.; Momeni, M. M. Flexible photo-assisted supercapacitor utilizing ternary Mn-Ni-Co sulfides on titania electrodes. *Chem. Eng. J.* **2025**, *507*, 160555.
(54) Boruah, B. D.; Wen, B.; De Volder, M. Molybdenum disulfide−Zinc oxide photocathodes for photo-rechargeable Zinc-ion batteries. *ACS Nano* **2021**, *15* (10), 16616−16624.
(55) Zheng, Z.; Ding, C.; Hasan, M. S.; Wang, K.; Liu, Y.; Yang, W.; Cheng, J.; Luo, Z.; Cao, S.; Ding, Y. In-situ study of photo-rechargeable aqueous Zinc-ion batteries with the bifunctional α-MnO_2 photoelectrodes. *Adv. Funct. Mater.* **2025**, *35* (41), 2500182.
(56) Han, J.; Lee, J.; Jang, E.; Kim, M.; Cha, H.; Jo, S.; Yoo, J. Portable integrated photo-charging storage device operating at 3 V. *Chem. Eng. J.* **2022**, *450*, 138463.
(57) Sun, X.; Lan, Z.; Wang, M.; Geng, Q.; Lv, X.; Li, M. Multifunctional role of Ag-substitution in enhancing the photoelectrochemical properties of $LaFeO_3$ photocathodes. *ChemSusChem* **2023**, *16* (20), No. e202300645.
(58) Cruz-Manzo, S.; Greenwood, P. An impedance model based on a transmission line circuit and a frequency dispersion Warburg component for the study of EIS in Li-ion batteries. *J. Electroanal. Chem.* **2020**, *871*, 114305.
(59) Zeng, Z.; Mei, B.-A.; Song, G.; Hamza, M.; Yan, Z.; Wei, Q.; Feng, H.; Zuo, Z.; Jia, B.; Xiong, R. Physical interpretation of the electrochemical impedance spectroscopy (EIS) characteristics for diffusion-controlled intercalation and surface-redox charge storage behaviors. *J. Energy Storage* **2024**, *102*, 114021.
(60) Sang, Y.; Cao, X.; Wang, L. X.; Ding, G. F.; Wang, Y. J.; Yu, D. S.; Hao, Y. N.; Li, L. L.; Peng, S. J. Facile synthesis of three-dimensional spherical $Ni(OH)_2$/$NiCo_2O_4$ heterojunctions as efficient bifunctional electrocatalysts for water splitting. *Int. J. Hydrogen Energy* **2020**, *45* (55), 30601−30610.
(61) Zhou, X.; Yue, X.; Dong, Y.; Zheng, Q.; Lin, D.; Du, X.; Qu, G. Enhancing electrochemical performance of electrode material via combining defect and heterojunction engineering for supercapacitors. *J. Colloid Interface Sci.* **2021**, *599*, 68−78.
(62) Yang, W.; Gao, Z.; Ma, J.; Zhang, X.; Wang, J.; Liu, J. Hierarchical $NiCo_2O_4$@NiO core−shell hetero-structured nanowire arrays on carbon cloth for a high-performance flexible all-solid-state electrochemical capacitor. *J. Mater. Chem. A* **2014**, *2* (5), 1448−1457.
(63) Guo, B.; Li, Y.; Gao, Y.; Zhao, S.; Li, Y.; Lv, X.; Mi, C.; Li, M. Strategy of voltage match on the maximum power point for a high-efficiency photorechargeable device. *ACS Appl. Mater. Interfaces* **2023**, *15* (9), 11875−11884.
(64) Zhang, F.; Li, W.; Xu, Z.; Ye, M.; Xu, H.; Guo, W.; Liu, X. Highly flexible and scalable photo-rechargeable power unit based on symmetrical nanotube arrays. *Nano Energy* **2018**, *46*, 168−175.
(65) Bi, J.; Zhang, J.; Giannakou, P.; Wickramanayake, T.; Yao, X.; Wang, M.; Liu, X.; Shkunov, M.; Zhang, W.; Zhao, Y. A Highly integrated flexible photo-rechargeable system based on stable ultrahigh-rate quasi-solid-state zinc-ion micro-batteries and perovskite solar cells. *Energy Storage Mater.* **2022**, *51*, 239−248.

https://doi.org/10.1021/acsami.6c02790
ACS Appl. Mater. Interfaces 2026, 18, 32546−32556